Rapid anatomical brain imaging using spiral acquisition and an expanded signal model

Kasper, Lars ; Engel, Maria ; Barmet, Christoph ; Haeberlin, Maximilian ; Wilm, Bertram J ; Dietrich, Benjamin E ; Schmid, Thomas ; Gross, Simon ; Brunner, David O ; Stephan, Klaas E ; Pruessmann, Klaas P

Abstract: We report the deployment of spiral acquisition for high-resolution structural imaging at 7T. Long spiral readouts are rendered manageable by an expanded signal model including static off-resonance and B0 dynamics along with k-space trajectories and coil sensitivity maps. Image reconstruction is accomplished by inversion of the signal model using an extension of the iterative non-Cartesian SENSE algorithm. Spiral readouts up to 25 ms are shown to permit whole-brain 2D imaging at 0.5 mm in-plane resolution in less than a minute. A range of options is explored, including proton-density and T2* contrast, acceleration by parallel imaging, different readout orientations, and the extraction of phase images. Results are shown to exhibit competitive image quality along with high geometric consistency.

DOI: https://doi.org/10.1016/j.neuroimage.2017.07.062

Rapid Anatomical Brain Imaging using Spiral Acquisition and an Expanded Signal Model

Lars Kasper[1,2], Maria Engel[1], Christoph Barmet[1,3], Maximilian Haeberlin[1], Bertram J Wilm[1], Benjamin E Dietrich[1], Thomas Schmid[1], Simon Gross[1], David O Brunner[1], Klaas E Stephan[2,4,5], Klaas P Pruessmann[1]

[1]Institute for Biomedical Engineering, ETH Zurich and University of Zurich, Zurich, Switzerland

[2]Translational Neuromodeling Unit, IBT, University of Zurich and ETH Zurich, Zurich, Switzerland

[3]Skope Magnetic Resonance Technologies AG, Zurich, Switzerland

[4]Wellcome Trust Centre for Neuroimaging, University College London, London, United Kingdom

[5]Max Planck Institute for Metabolism Research, Cologne, Germany

Additional Submission Info

- Submission to special issue:

Neuroimaging with Ultra-High Field MRI: Present and Future

Editors: Jonathan R. Polimeni, Kâmil Uludağ

Highlights

- Whole-brain high resolution T_2* and PD images (0.5x0.5x2mm^3) are acquired at 7T in less than 1min using 2D spiral readouts.
- This represents a 5-10x acceleration compared to spin-warp imaging, with competitive image quality and geometric accuracy.
- An expanded signal model and iterative reconstruction proved essential to harness long spiral readout segments (25 ms).

- The signal model accounts for static and dynamic off-resonance, actual gradient dynamics, and coil sensitivity encoding.
- Accurate measurement of all model components was crucial, with field dynamics being concurrently monitored by NMR probes.

ABSTRACT

We report the deployment of spiral acquisition for high-resolution structural imaging at 7T. Long spiral readouts are rendered manageable by an expanded signal model including static off-resonance and B_0 dynamics along with k-space trajectories and coil sensitivity maps. Image reconstruction is accomplished by inversion of the signal model using an extension of the iterative non-Cartesian SENSE algorithm. Spiral readouts up to 25 ms are shown to permit whole-brain 2D imaging at 0.5 mm in-plane resolution in less than a minute. A range of options is explored, including proton-density and T2* contrast, acceleration by parallel imaging, different readout orientations, and the extraction of phase images. Results are shown to exhibit competitive image quality along with high geometric consistency.

1 INTRODUCTION

The utility of MRI depends critically on how fast it can be performed. Patient comfort and compliance, patient throughput, and robustness against motion all relate directly to the duration of MR exams. The time needed for a given scan generally depends on the amount of data required and the efficiency of data collection. The former mostly reflects basic parameters like the number of slices, the field of view, and the targeted resolution. The scanning efficiency, on the other hand, is governed by the speed of k-space traversal, potential undersampling as in parallel imaging, and the acquisition duty cycle, i.e., the fraction of total sequence duration actually spent collecting data. The duty cycle is lessened by the sequence overhead, i.e., by all time spent on purposes other than acquisition such as RF excitation, preparation pulses, or gradient spoiling. Standard spin-warp sequences (commercially known as FFE, GE, GRE, among others) tend to exhibit low acquisition duty cycles since they sample only one k-space line per excitation. Their relative inefficiency is exacerbated by contrast preparation, e.g., by long echo times for T2 or T2* weighting or by diffusion weighting with large gradient moments.

52 The acquisition duty cycle can generally be improved by expanding acquisition windows. A
53 prominent example of this approach is echo-planar imaging (EPI, Mansfield, 1977), which
54 samples multiple k-space lines per repetition. Single-shot EPI is frequently employed for
55 diffusion imaging, BOLD fMRI and spin-labeling studies. Multi-shot EPI has recently been used
56 for high-resolution anatomical imaging with T2* and phase contrast (Langkammer et al., 2015;
57 Poser et al., 2015; Setsompop et al., 2016; Zwanenburg et al., 2011).

58 The most efficient extended readouts, however, are accomplished with spiral trajectories (Ahn et
59 al., 1986; Likes, 1981), which feature substantially higher average k-space speed than EPI.
60 Spiral trajectories offer minimal echo times and mitigation of motion and flow effects by intrinsic
61 compensation of gradient moments (Meyer et al., 1992). Spiral imaging also achieves near-
62 optimal SNR efficiency by spreading acquisition time approximately evenly across k-space
63 (Kasper et al., 2014) and has been successfully accelerated by array detection (Heberlein and
64 and Hu, 2006; Heidemann et al., 2006; Pruessmann et al., 2001; Yeh et al., 2005). Recently,
65 extensions of spiral imaging to 3D and simultaneous multi-slice excitation have been
66 demonstrated (Deng et al., 2016; Zahneisen et al., 2014), enabling further acceleration.

67 Despite these attractive features, spiral imaging is not commonly used in applied settings due to
68 a number of challenges as summarized, e.g., in Refs. (Block and Frahm, 2005; Börnert et al.,
69 1999). Out of those, the most prominent issues relate to imperfections of the static magnetic field
70 and dynamic gradient fields. Static field non-uniformity, when uncorrected, causes blurring in
71 spiral scans as opposed to EPI where it induces mere distortions. One means of controlling off-
72 resonance effects is to limit the readout duration in a trade-off between image quality and
73 acquisition efficiency (Qian et al., 2010). At the image reconstruction stage, the off-resonance
74 problem is traditionally addressed by variants of conjugate-phase reconstruction, a direct
75 approach that works within certain limits on the spatial derivatives of the static field (Maeda et
76 al., 1988; Man et al., 1997; Noll et al., 1992, 1991). More general cases have been tackled with
77 iterative algorithms for full-Fourier encoding (Barmet et al., 2004; Harshbarger and Twieg, 1999;
78 Sutton et al., 2003) and parallel imaging with undersampling and array detection (Barmet et al.,
79 2005; Wilm et al., 2011).

80 The second main issue, imperfections of gradient dynamics, arises from eddy currents, delays,
81 mechanical vibrations, and heating effects, among others. In EPI, many system imperfections

can be addressed with calibration echo trains, exploiting the repetitive structure of the readout gradient waveform. For spiral readouts, lacking such structure, a generic approach is to measure the entire k-space trajectory using MR signal from a phantom or the subject (Duyn et al., 1998) or specific probes (Barmet et al., 2008; Börnert et al., 1999; De Zanche et al., 2008; Mason et al., 1997). To also capture transient field behavior related to, e.g., thermal drift, system instability, or subject motion, it has recently been proposed to perform trajectory and eddy current measurements concurrently with each actual imaging readout (Barmet et al., 2009; Vannesjo et al., 2015).

Joint correction for off-resonance and trajectory errors has recently been shown to facilitate single-shot spiral imaging at 3T (Wilm et al., 2017). In this work, simultaneous accounting for static and dynamic field perturbations was based on an expanded signal model that additionally encompassed array detection. Image reconstruction was achieved by model inversion using an extension of the iterative non-Cartesian SENSE algorithm (Pruessmann et al., 2001; Wilm et al., 2015, 2011). Based on these results the goal of the present work is to explore the feasibility of spiral scanning at even higher field. Moving to 7T offers additional intrinsic SNR for scan acceleration but also exacerbates the off-resonance challenge. We demonstrate that spiral scanning enables rapid structural imaging in these conditions. Using array acquisition and up to threefold undersampling, whole-brain imaging with 0.5 mm in-plane resolution is accomplished in less than one minute and with high geometric fidelity.

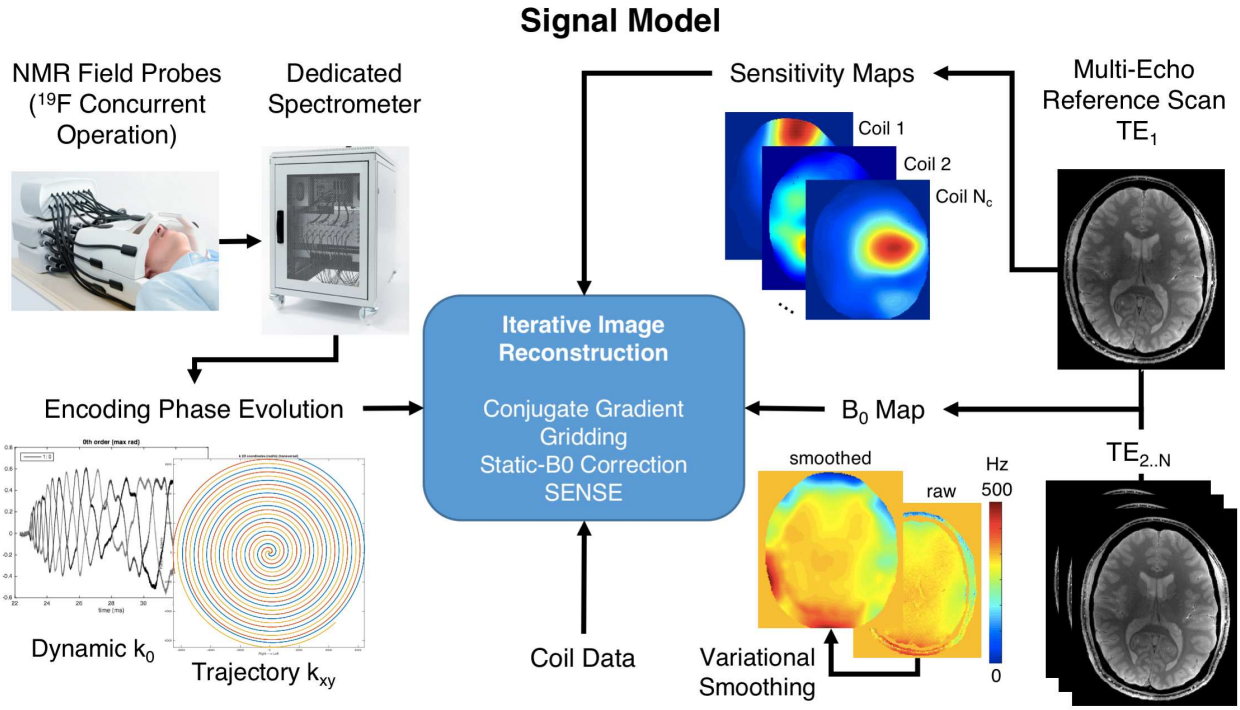

***Figure 1**: Image formation based on the expanded signal model given in Eq. [1]. Raw image data is complemented by concurrently measured field dynamics as well as maps of receiver sensitivity and static B_0. Algebraic image reconstruction inverts the signal model using a conjugate gradient algorithm.*

2 METHODS

2.1 Setup and Subjects

All experiments were performed on a 7T Philips Achieva system (Philips, Best, The Netherlands) using a 32-channel head receive array (Nova Medical, Wilmington, USA). Data was collected from 4 healthy volunteers (1 male, mean age 24 ± 2 y) after written informed consent and according to the applicable ethics approval.

Field data was acquired using a concurrent magnetic field monitoring setup similar to previous 3T implementations (Barmet et al., 2009; Wilm et al., 2011). The front-end comprised 16 ^{19}F NMR field probes (De Zanche et al., 2008) with the following properties: inner capillary/droplet diameter 0.8mm, hexafluorobenzene filling, $T_1 \approx 70$ ms (doped with 50 mmol/l $Cr(TMHD)_3$). For operation concurrent with ^{1}H imaging the probe heads were RF-shielded and cables were equipped with cable traps. The probes were mounted between the receive array and the surrounding transmit coil. The set of probe positions was optimized for minimum noise propagation from probe signals into the field model (Barmet et al., 2010), accounting for the conditioning of the probe-position-dependent calibration matrix (Barmet et al., 2008). The space of feasible probe positions was created from numerical 3D models of the transmit coil and the receive array.

The probes were connected to a stand-alone console and acquisition system (Dietrich et al., 2016a). To synchronize imaging and field measurements the clock of the monitoring spectrometer was locked to that of the imaging system and the delay difference between the two systems was corrected for. One-time delay calibration was based on the phase of spin-warp images and ghosting levels in single-shot EPI images.

Processing of field probe data was performed on a PC. The acquired signal phase evolutions of 1 MHz bandwidth were projected onto a spherical harmonic basis set (Barmet et al., 2008; Vannesjo et al., 2013; Wilm et al., 2011), yielding coefficient time courses for global phase (k_0), first-order k-space (k_x, k_y, k_z), as well as second- and third-order spatial components ($k_4, \dots k_{15}$). Correction for concomitant gradient fields was incorporated by modeling them from the monitored first-order phase terms and subtracting their effects from the probe phase data before re-estimating the phase coefficients ($k_0, \dots k_{15}$) (Bernstein et al., 1998; Vannesjo et al., 2016b).

2.2 Spiral Trajectories and Sequence Timing

For spiral scanning two protocols were used in this study, with 0.5 mm and 0.7 mm nominal in-plane resolutions, respectively, and a common FOV of 230 mm (see Table 1 for an overview of sequence parameters). The spiral readout modules were embedded in 2D multi-slice gradient-

138 echo sequences targeting whole-brain coverage (36 oblique-transverse slices of 2-3 mm
139 thickness, 0.5-1 mm gap) with a volume TR of 3 s.

Table 1: *Sequence parameters of 2D spiral trajectories used in this study. All of the below sequences shared an in-plane FOV of 230 mm, acquired 36 transverse slices of 2-3 mm thickness, and a TR of 3 s. For the variants, only fields with deviating parameters were entered. The SENSE3/4 variants were retrospectively undersampled from the corresponding full dataset.*

Protocol	Variant	In-plane Resolution (mm)	Number of Interleaves	TE (ms)	Readout Direction	Readout Duration Per Shot (ms)	SENSE Factor	Total Scan Duration (s)
High-Resolution	T2*	0.5	30	25	spiral-out	20	1	90
	T2*-in		30	25	spiral-in		1	90
	PD		30	5	spiral-out		1	90
	SENSE3		10	25	spiral-out		3	30
High-Speed	T2*-out	0.7	12	25	spiral-out	25	1	36
	T2*-in		12	29	spiral-in		1	36
	SENSE4-out		4	25	spiral-out		4	9
	SENSE4-in		4	29	spiral-in		4	9

140

141 All spiral readout trajectories were Archimedean (radially equidistant turns), directed either
142 center-out ("spiral-out") or towards the k-space center after an initial prephaser ("spiral-in").

143 Segmented k-space sampling was performed with spiral interleaves of up to 25 ms readout
144 duration. The respective gradient waveforms were designed to make full use of the gradient
145 system's slew-rate and strength limits of 200 mT/m/ms and 31 mT/m, respectively (Lustig et al.,
146 2008). For the given FOV, full k-space coverage required 30 interleaves for the 0.5 mm protocol
147 and 12 interleaves for the 0.7 mm protocol, resulting in total scan durations of 90 s and 36 s,
148 respectively.

For contrast variation, the spiral readout module was shifted relative to slice excitation, with nominal echo time (TE) indicating the sampling time of the k-space center (Fig. 2), i.e., marking the end of the readout for spiral-in trajectories. For T2* weighting TEs of 20-29 ms were employed for spiral-out and -in trajectories. In addition, a variant of the spiral-out scan with short TE (5 ms) served to explore more proton-density-weighted (PD) contrast. SPIR fat suppression (Kaldoudi et al., 1993) preceded each imaging module.

Field-probe excitation and acquisition were triggered by the MR console 3 ms before onset of the respective spiral waveforms (Fig. 2b, bottom). After excitation with a block pulse, monitoring signals were collected over the whole spiral readout at a bandwidth of 1 MHz. To allow for probe T1 recovery, monitoring was performed only for a subset of readouts spaced at 200-300 ms and thus still critically sampling breathing-induced field changes (Duerst et al., 2015; Van de Moortele et al., 2002; Vannesjo et al., 2015). Depending on sequence timing, this amounted to concurrent monitoring of every 2nd to 6th slice.

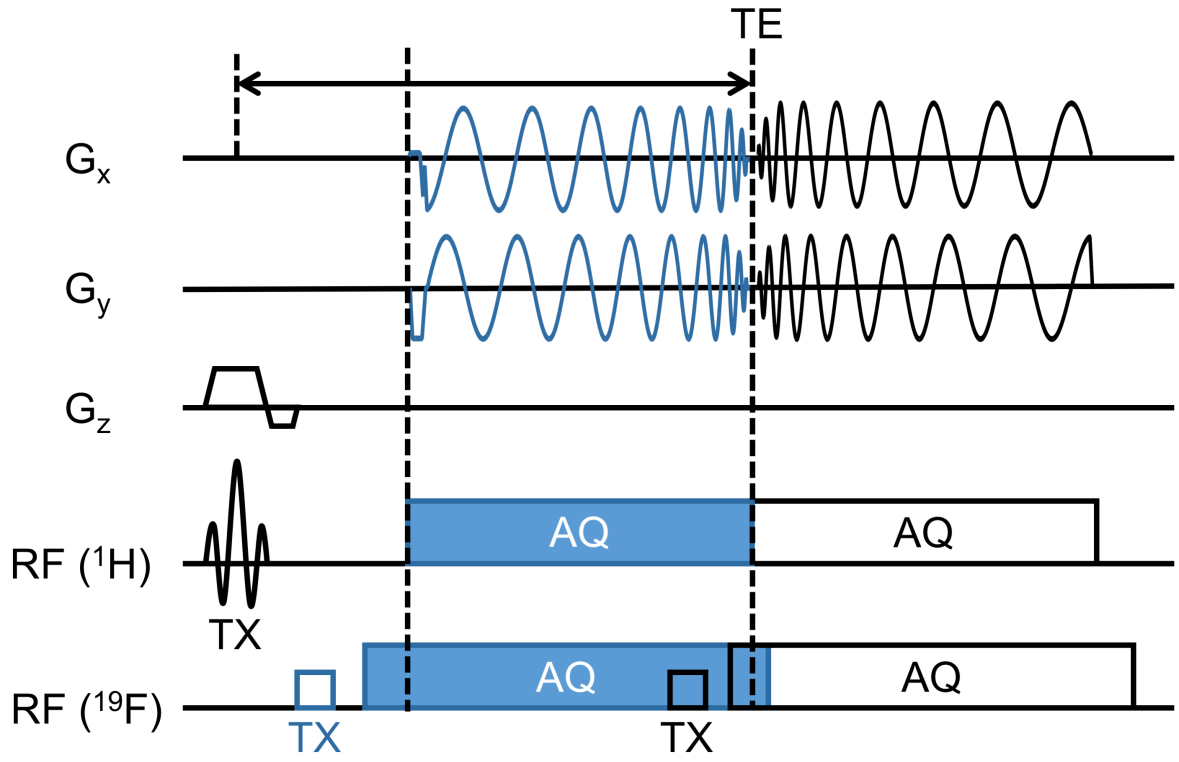

***Figure 2**: Sequence diagram.*

Spiral-In (blue) and spiral-out (black) trajectory and accompanying excitation/acquisition scheme for concurrent field monitoring with ^{19}F probes. Note that spiral-in and -out have the same nominal echo time (TE) here. A third trajectory (not shown) with short TE (PD-weighting) was employed by shifting the onset of the spiral-out module to the displayed start of the spiral-in trajectory.

2.3 Reference Maps: Sensitivity and Static Off-resonance

For mapping of coil sensitivity and static off-resonance a spin-warp multi-gradient-echo sequence (TE_1 = 4 ms, ΔTE = 1ms, 6 echoes, TR = 800 ms, 1 mm resolution) was employed with the same slice geometry as the anatomical scans. For geometric consistency (Wilm et al., 2015) the reference scan was likewise concurrently monitored and reconstructed based on the

expanded signal model described in the following section, albeit without reference map data and individually for each receive channel.

Coil sensitivity maps were created from the first-echo data, dividing each single-channel image by the root of the sum of the squared magnitude over all channels. Sensitivity-weighted complex channel combination yielded complex images for each of the six echoes (Roemer et al., 1990). Static off-resonance maps were generated from these multi-echo images by pixel-wise temporal unwrapping and linear fitting of the image phase along the echo dimension.

Noise and voids in both types of maps were removed with a variational approach similar to that described in Ref. (Bammer et al., 2002). It consists in minimizing an objective function that penalizes a map's deviation from raw values along with its second spatial derivatives. Minimization was performed with a conjugate gradient algorithm (Shewchuk, 1994).

2.4 Expanded Signal Model and Image Reconstruction

The expanded signal model (Fig. 1) was detailed previously (Barmet et al., 2005; Wilm et al., 2011). In brief, the raw image signal acquired with coil γ at time t is described as a function of available magnetization $m(\boldsymbol{r})$, $\boldsymbol{r}$ denoting position, the phase model $\varphi(\boldsymbol{r},t)$ obtained by monitoring, coil sensitivity $c_\gamma(\boldsymbol{r})$, and static off-resonance $\Delta\omega(\boldsymbol{r})$:

$$s_\gamma(t) = \int_V m(\boldsymbol{r}) \cdot c_\gamma(\boldsymbol{r}) \cdot \mathrm{e}^{i\varphi(\boldsymbol{r},t)}\, \mathrm{e}^{i\Delta\omega(\boldsymbol{r})t}\, \mathrm{d}\boldsymbol{r} \qquad [1]$$

Discretizing time and space yields the matrix-vector formulation (Pruessmann, 2006; Pruessmann et al., 1999)

$$\boldsymbol{s} = E\,\boldsymbol{m} \qquad [2]$$

with the encoding matrix

$$E_{(\gamma,\tau),\rho} = c_\gamma(\boldsymbol{r}_\rho)\ \mathrm{e}^{i\left(k_0(t_\tau) + \boldsymbol{k}(t_\tau)\cdot\boldsymbol{r}_0 + \boldsymbol{k}(t_\tau)\cdot(\boldsymbol{r}_\rho - \boldsymbol{r}_0)\ +\ \varphi_{ho}(\boldsymbol{r}_\rho,t_\tau)\right)}\ \mathrm{e}^{i\Delta\omega(\boldsymbol{r}_\rho)t_\tau}\,, \qquad [3]$$

the indices τ, ρ counting sampling time points and voxel positions, respectively. The voxel positions $\boldsymbol{r}_\rho$ were decomposed into a vector $\boldsymbol{r}_0$ pointing to the slice center and the in-plane component $(\boldsymbol{r}_\rho - \boldsymbol{r}_0)$. The monitoring result $\varphi(\boldsymbol{r}, t)$ was decomposed here into the spatially uniform phase, k_0, spatially linear phase, $\boldsymbol{k} \cdot \boldsymbol{r}$, and higher-order terms φ_{ho} of the spherical harmonic basis set.

In this formulation, image reconstruction amounts to solving the matrix equation. This is achieved with the iterative conjugate-gradient SENSE algorithm (Pruessmann et al., 2001), extended as in Ref. (Kasper et al., 2014). Each iteration requires multiplication of the encoding matrix, E, and its adjoint, E^H, with temporary vectors. The matrix-vector multiplications are rendered efficient by several measures. Multiplications by $c_\gamma(\boldsymbol{r})$ and $e^{ik_0(t)}e^{i\boldsymbol{k}(t)\cdot\boldsymbol{r}_0}$ are performed in the spatial and time domains, respectively, where they amount to diagonal operations. Multiplication with $\mathrm{e}^{\pm i\boldsymbol{k}(t_\tau)\cdot(\boldsymbol{r}_\rho - \boldsymbol{r}_0)}$ and summation over ρ and τ, respectively, are performed by reverse and forward gridding and FFT (Beatty et al., 2005; Jackson et al., 1991; Pruessmann et al., 2001). The off-resonance factor $e^{i\Delta\omega_0(\boldsymbol{r}_\rho)t_\tau}$ is incorporated by multi-frequency interpolation (Barmet et al., 2005; Man et al., 1997; Sutton et al., 2003). Normalization for net sensitivity of the coil array and estimated k-space density are used for pre-conditioning (Pruessmann et al., 2001). Higher-order phase, $\varphi_{ho}(\boldsymbol{r}_\rho, t_\tau)$, is measured in the present work but neglected at the reconstruction stage due to small magnitude and reconstruction speed. When significant, higher-order fields can be incorporated in the CG approach (Wilm et al., 2017, 2015, 2012, 2011), yet at the expense of additional computation, as gridding and FFT speed-up are no longer possible. Image reconstruction was implemented in Matlab (The MathWorks, Natick, MA), using its distributed computing engine on a CPU cluster with dedicated server nodes (Dual Deca-Core Intel Xeon E5-2690 v2 3GHz CPUs, 20 cores per node). Up to 32 cores were employed for reconstructions. SENSE reconstruction of the fully sampled data took about 40 s per iteration for an individual slice (matrix size 380x460), amounting to a total reconstruction time of just under 7 minutes (10 iterations). Alternatively, without undersampling, magnitude-only images could be computed from root sum of square combinations of individual coil reconstructions, taking 12 s per iteration on a single core, thus allowing total reconstruction times of 2 min by parallelization over coils.

To explore further acceleration of spiral acquisition by parallel imaging, image reconstructions were repeated using only 10 of the acquired 30 interleaves of the 0.5 mm resolution spiral sequences (SENSE factor 3, total scan time 30 s), and every 4th interleaf of the 0.7 mm resolution sequences (SENSE factor 4, total scan time 9 s).

After reconstruction all images were corrected for intensity modulations of low spatial order due to the coil profiles, estimated as bias field with the unified segmentation approach (Ashburner and Friston, 2005) in SPM12 (www.fil.ion.ucl.ac.uk/spm/software/spm12/).

3 RESULTS

3.1 Field Dynamics During Spiral Readouts

Field evolutions during spiral encoding with k-space range corresponding to 0.5 mm resolution were successfully monitored as illustrated by the example in Fig. 3, a T2*-weighted spiral-out trajectory (TE 25 ms). The first-order phase components (Fig. 3B) reflect the intended, slightly angulated spiral trajectory. Deviations from the nominal trajectory (dashed) include slightly reduced maxima and apparent negative delays, which relate to frequency-dependent system response. B_0 eddy currents are manifest in k_0, which varies in the order of 1 rad (Fig. 3A). Higher-order dynamics were generally smaller (Fig. 3CD) with the exception of 2nd-order concomitant fields (Fig. 3C), in particular in z^2 (Bernstein et al., 1998). Different interleaves exhibit similar field dynamics yet with phase-shifted oscillating components due to different rotation relative to the gradient system (right column, only every third interleaf is shown for clearer visualization). Less systematic differences among interleaves are most apparent in high spatial order and towards the end of the readout.

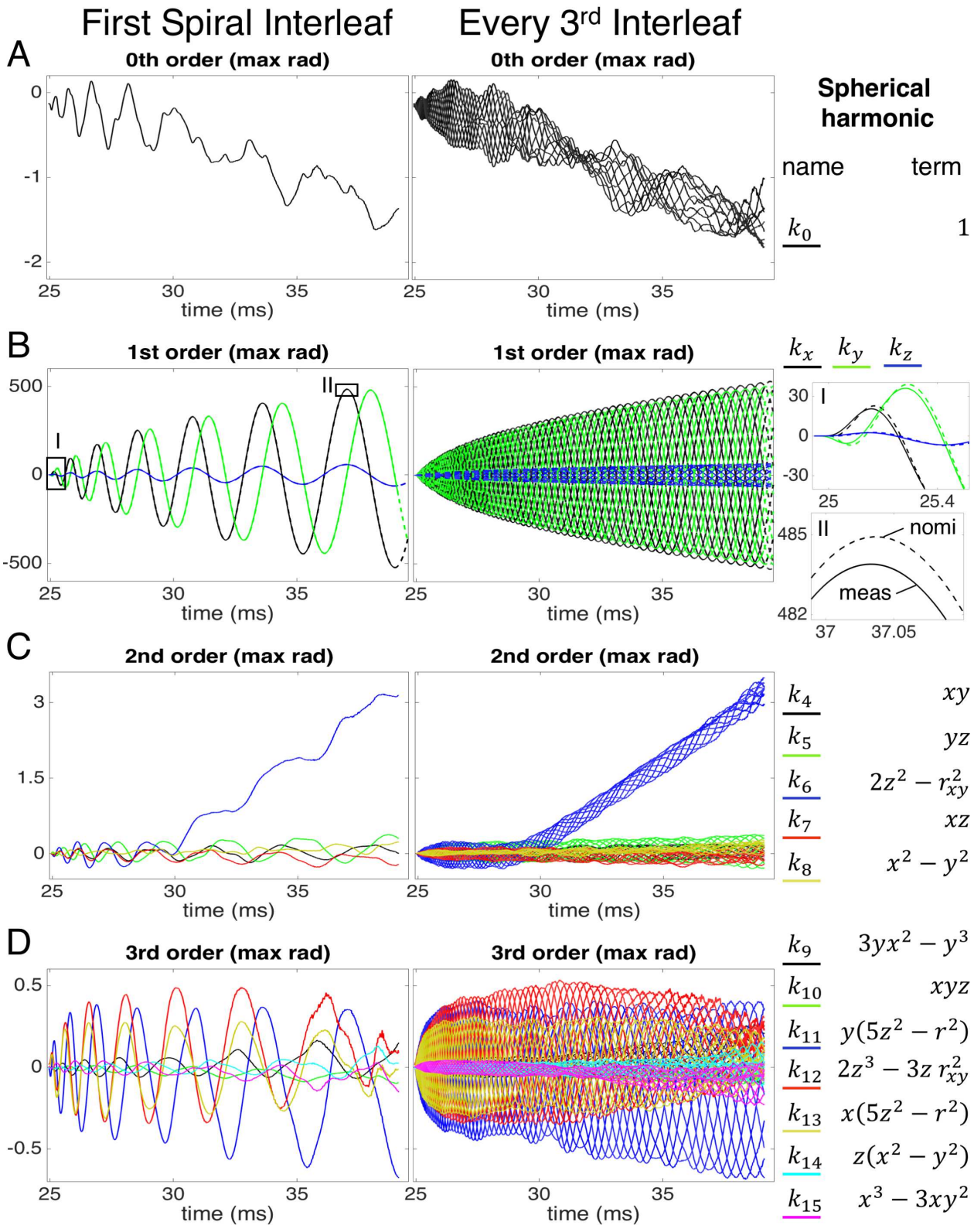
First Spiral Interleaf
Every 3rd Interleaf
A
0th order (max rad)
0th order (max rad)
0
-1
-2
25
30
35
time (ms)
Spherical harmonic
name
term
k_0
1
B
1st order (max rad)
1st order (max rad)
500
0
-500
I
II
k_x k_y k_z
30
0
-30
25
25.4
485
482
nomi
meas
37
37.05
C
2nd order (max rad)
2nd order (max rad)
3
1.5
0
k_4 xy
k_5 yz
k_6 $2z^2 - r_{xy}^2$
k_7 xz
k_8 $x^2 - y^2$
D
3rd order (max rad)
3rd order (max rad)
0.5
0
-0.5
k_9 $3yx^2 - y^3$
k_{10} xyz
k_{11} $y(5z^2 - r^2)$
k_{12} $2z^3 - 3z\,r_{xy}^2$
k_{13} $x(5z^2 - r^2)$
k_{14} $z(x^2 - y^2)$
k_{15} $x^3 - 3xy^2$

***Figure 3**: Monitored phase evolution during spiral-out encoding (TE 25 ms). Maximum phase excursion in a sphere of 10 cm radius ("max rad") is shown for different spatial orders of spherical harmonics (rows). Left: First interleaf (of 30); right: Every third interleaf shown, illustrating (in)consistency across spiral segments. (A) Zeroth-order (uniform) phase evolution, including eddy-current effects. Static field offsets appear as a slope. (B) Monitored (solid line, "meas") and nominal k-space trajectory (dashed line, "nomi"). The measured spiral exhibits negative delays and reduced maximum excursions (zooms I and II on the right, indicated by black boxes). (C) Second-order spherical harmonic phase terms. The dominant contribution in z^2 (blue) stems from a concomitant field induced by the spiral gradient waveform prevailing in the x-y gradient channels. (D) Third-order spherical harmonic basis terms exhibiting small-amplitude sinusoidal oscillation along with the spiral trajectory.*

3.2 High-resolution Spiral Images

Figure 4 shows reconstructed T2*-weighted spiral-out images (resolution 0.5 mm, scan time 90 s), which exhibit competitive structural image quality without conspicuous spiral artifacts. Consistent contrast and level of detail were obtained in all 36 slices (Fig. 4AB), including typical T2* emphasis of venous vasculature (Fig. 4D,H) and gray/white matter delineation (e.g., Fig. 4C,G). Notably, image quality is high also in low slices (4E,F), showing subcortical white matter (e.g., optical tract, Fig. 4D,H) and deep gray matter structures (e.g., putamen, globus pallidus, Fig. 4C,G). Local through-plane dephasing and consequent signal loss in these slices (Fig. 4F) relate to T2* weighting rather than the choice of trajectory (see short-TE images in Fig. 5A for comparison).

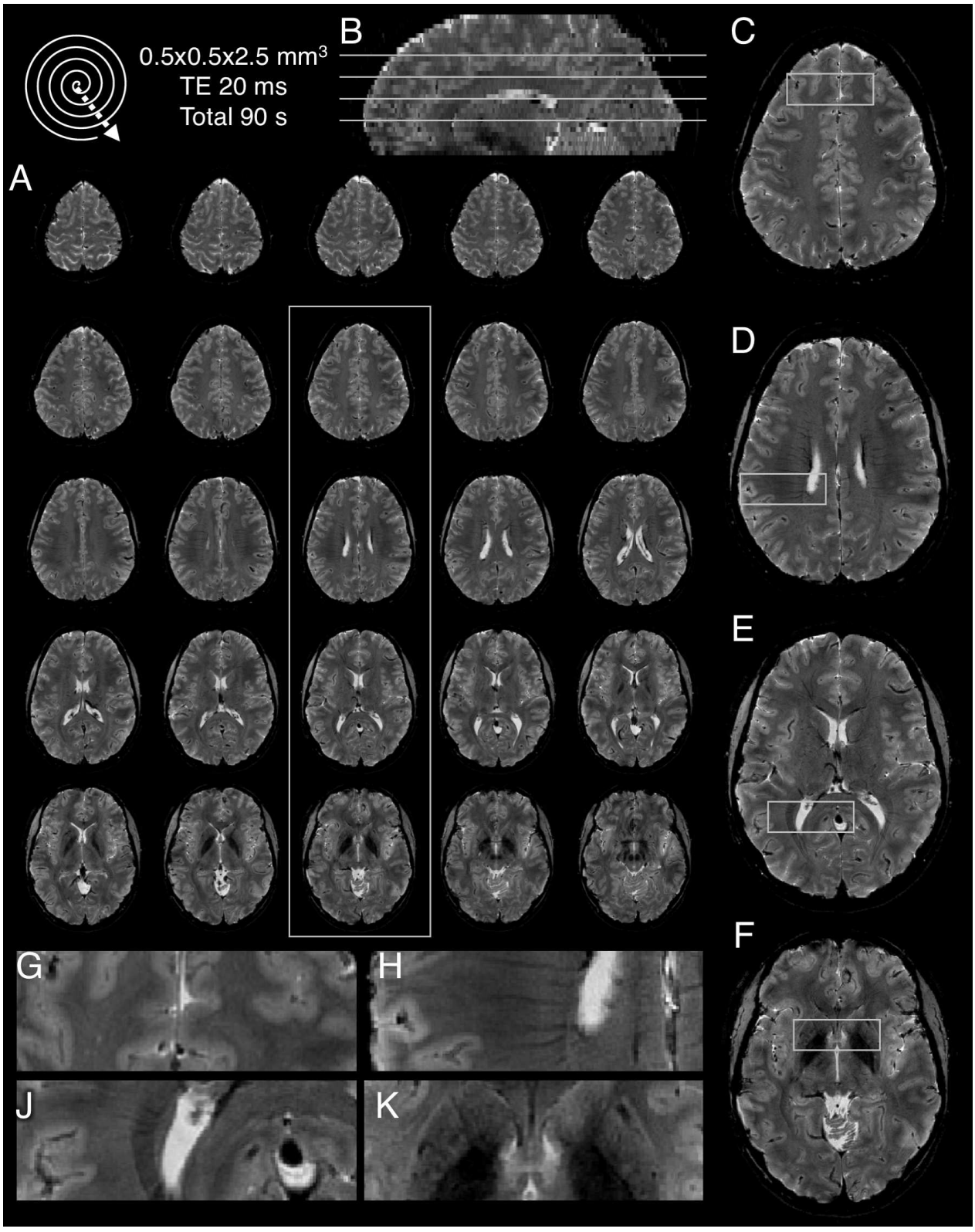
0.5x0.5x2.5 mm3
TE 20 ms
Total 90 s
A
B
C
D
E
F
G
H
J
K

Figure 4: *Spiral-out, T2*-weighted anatomical image (TE 25 ms). The whole dataset was acquired in 90 seconds without parallel-imaging acceleration. (A) Central 25 of the acquired 36 slices. White frame indicates selected slices for zoom (C-F). (B) Sagittal view of all slices, depicting coverage. White lines show positions of slices shown in (C-F). (C-F) Selected slices, superior to inferior, spaced by 17.5 mm. White boxes refer to zooms (G-K) in same alphabetical order. (G-K) Zooms of different slices, exemplifying the degree of anatomical detail, e.g. (G) overall gray/white matter contrast, (H) vasculature, (J) white-matter structures (optical tract) and (K) subcortical gray matter (putamen, globus pallidus).*

252

253 Similar image quality was obtained with the other trajectory and timing variants (Fig. 5). The
254 spiral-out trajectory with shorter TE (5 ms) yielded higher SNR and more pronounced proton-
255 density weighting, resulting in superior cortical gray/white matter contrast (Fig. 5A). Deep gray
256 matter and CSF contrast, on the other hand, is reduced (compare Fig. 5A to Figs. 5C or 4).
257 Slight ringing in these images may arise from residual fat signal after incomplete suppression,
258 that was not observed at longer TE due to fast T_2^* decay.

259 The spiral-in trajectory shared gradient timing with the short-TE spiral-out but, due to the
260 reversed trajectory direction, had a resulting TE of 25 ms, leading to predominantly T2* weighted
261 images (Fig. 5B). Overall, image contrast and quality were comparable to the spiral-out
262 trajectory with the same TE (cf. Fig. 4) in the corresponding slices (Fig. 5C). Subtle differences
263 were found in the manifestation of through-plane dephasing in inferior slices (Fig. 5B left) and in
264 the appearance of very local structures, particularly of small vessels (Fig. 5B, column 3).

265 Parallel imaging acceleration (R=3) preserved the contrast and anatomical detail pronounced by
266 T2* weighting. Apart from expected noise enhancement the undersampled data is comparable
267 with the fully sampled acquisition (compare Fig. 5D to C).

268 For all data presented in Fig. 5, a close-up of a different slice is provided in Fig. 6 to facilitate
269 comparison and detection of the aforementioned image features. Additional NIfTI images of the
270 other volunteers are provided as accompanying Data In Brief article (Kasper et al., 2017). In
271 general, the image quality between subjects was comparable, with individual differences close to

the sinuses due to through-plane dephasing, and at cortex edges close to the skull, because of steep in-plane static B0 gradients.

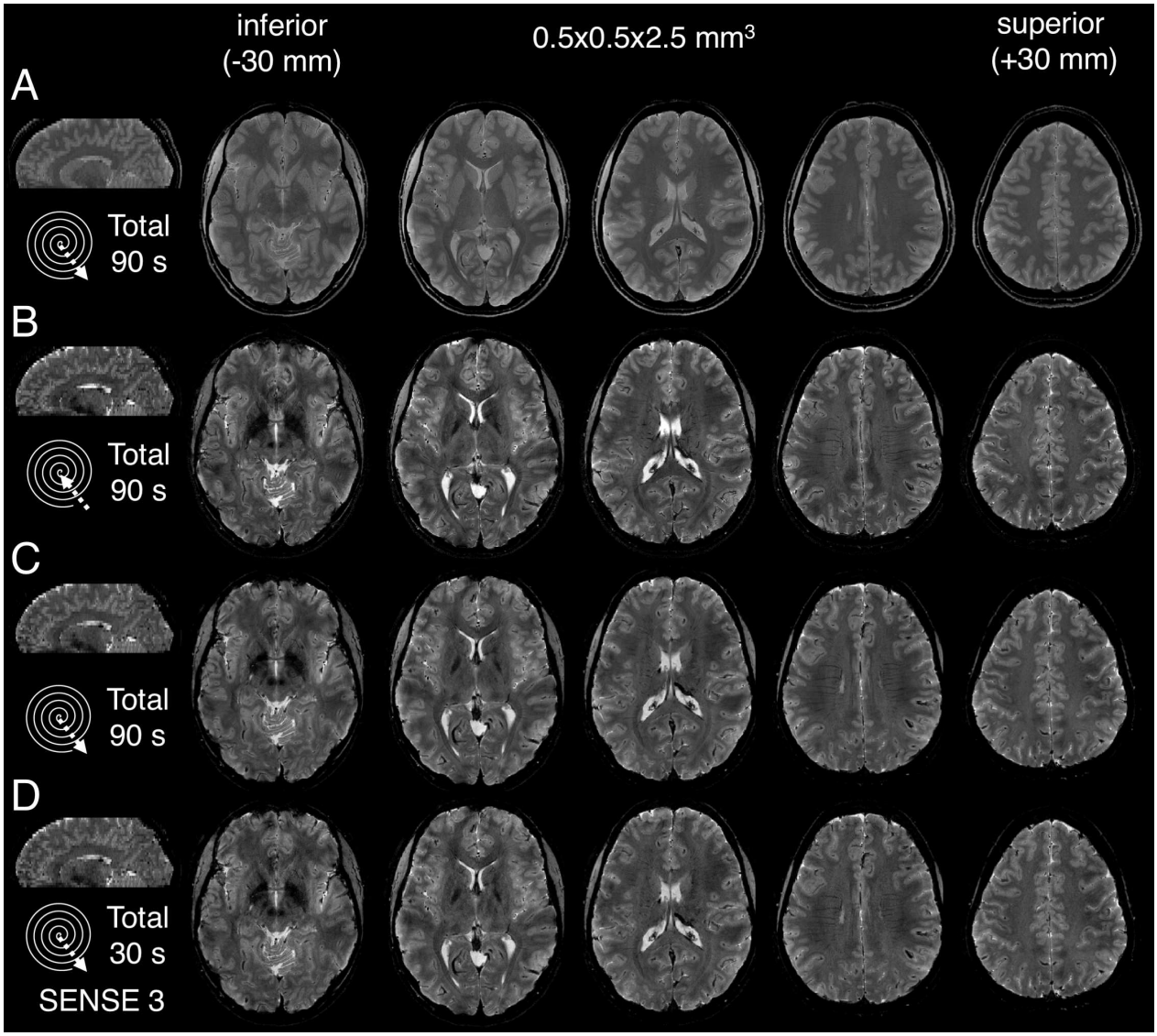

Figure 5: *Images reconstructed from different spiral acquisitions in the same session (shared*

parameters: 36 slices à 2.5 mm, slice gap 1 mm, TR 3 s, 30 interleaves a 20 ms readout duration). 5 oblique transverse slices are displayed, spaced by 17.5 mm, together with a sagittal view through all slices to depict coverage. (A) Spiral-out, TE 5 ms, depicting mixed proton-density and T2 weighting with high gray/white matter contrast; whole brain coverage in 90 s = 30 x TR. (B) Spiral-in, TE 25 ms, i.e., same gradient onsets as above, but reversed spiral readout direction. (C) Spiral-out, TE 25 ms. T2* weighting with global similarity to spiral-in, but locally more pronounced dephasing. (D) Spiral-out, TE 25 ms. As (C), but using only 10 interleaves for image reconstruction (SENSE=3), yielding whole brain coverage in only 30 s. Expected noise enhancement, but contrast and detail comparable to (C).*

277

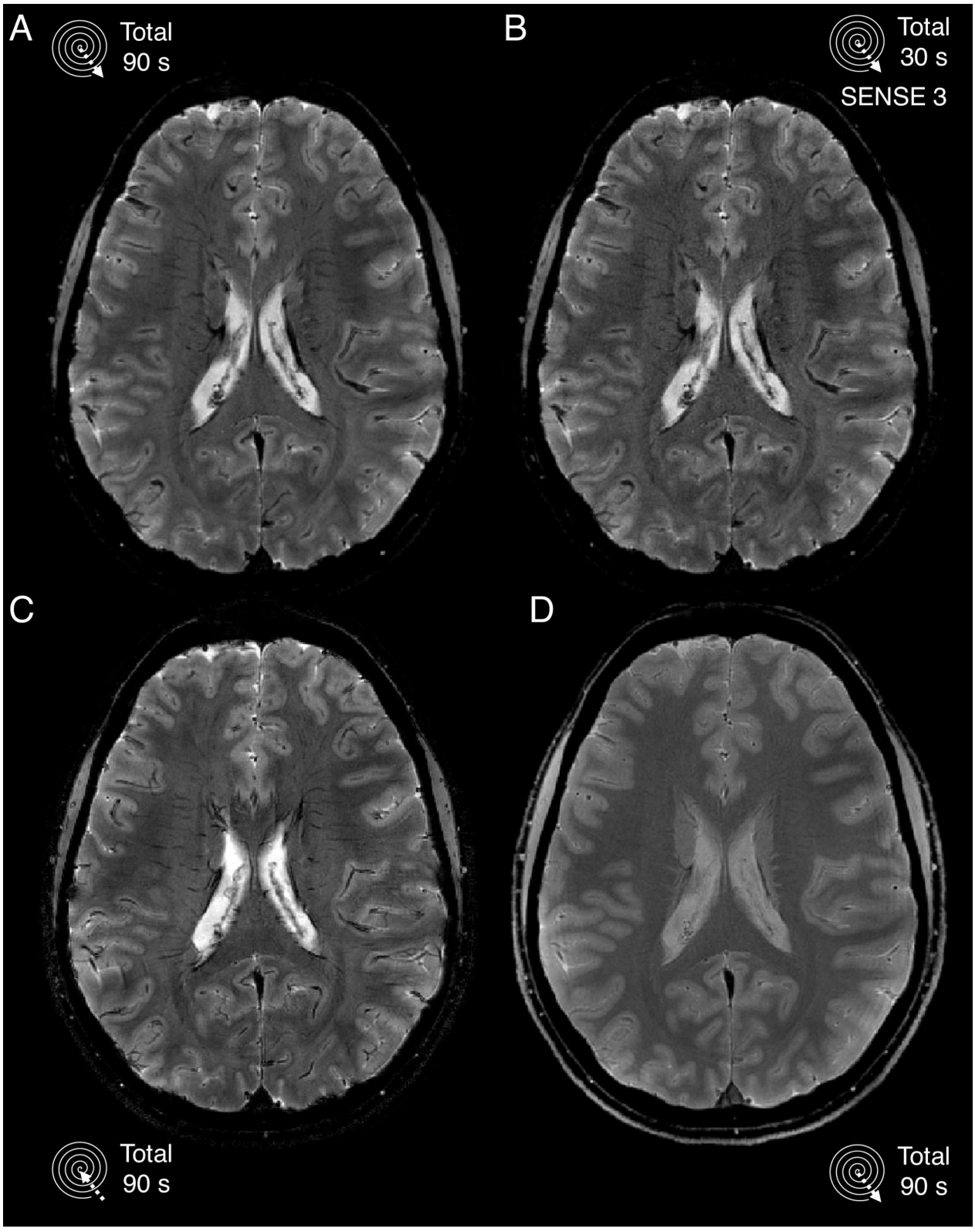
A
Total
90 s
B
Total
30 s
SENSE 3
C
Total
90 s
D
Total
90 s

Figure 6: *Close-up of contrast variants for the same scans as in Fig. 5, but a different slice. (A) Spiral-out, 0.5 mm, TE 25 ms; (B) Spiral-in, 0.5 mm, TE 25 ms; (C) Spiral-out, 0.5 mm, TE 25 ms – as (A), but only 10 interleaves employed for reconstruction (SENSE=3); (D) Spiral-out, 0.5 mm, TE 5 ms. Note subtle contrast differences visible in the zoomed view, e.g., the vessel depiction in spiral-in and -out.*

3.3 Geometric Fidelity and Impact of Signal Model Components

We compared the geometric consistency of the spiral results to the first echo images of the large-bandwidth spin-warp reference scan with minimal distortion (Fig. 7A). Visual inspection suggested good correspondence of anatomical structures in the short- and long-TE spiral-out scan to the spin-warp image at the level of 1 mm resolution (Fig. 7A, top row). The overlaid tissue boundaries (intensity edges) of the spin-warp image verify the geometric consistency for both spirals in in the transverse slices, as well as the sagittal through-plane geometry (Fig. 7A, bottom row).

To study the influence of off-resonance correction we repeated image reconstruction without incorporation of the off-resonance map (Fig. 7B). Compared to the static-B0-informed reconstruction, images without B0 correction exhibited tissue edge duplication and extended signal voids in areas of spatially varying B0 (Fig. 7B, bottom row, zoomed panels). We observed differences in image intensity of up to 20 %, mostly at tissue boundaries.

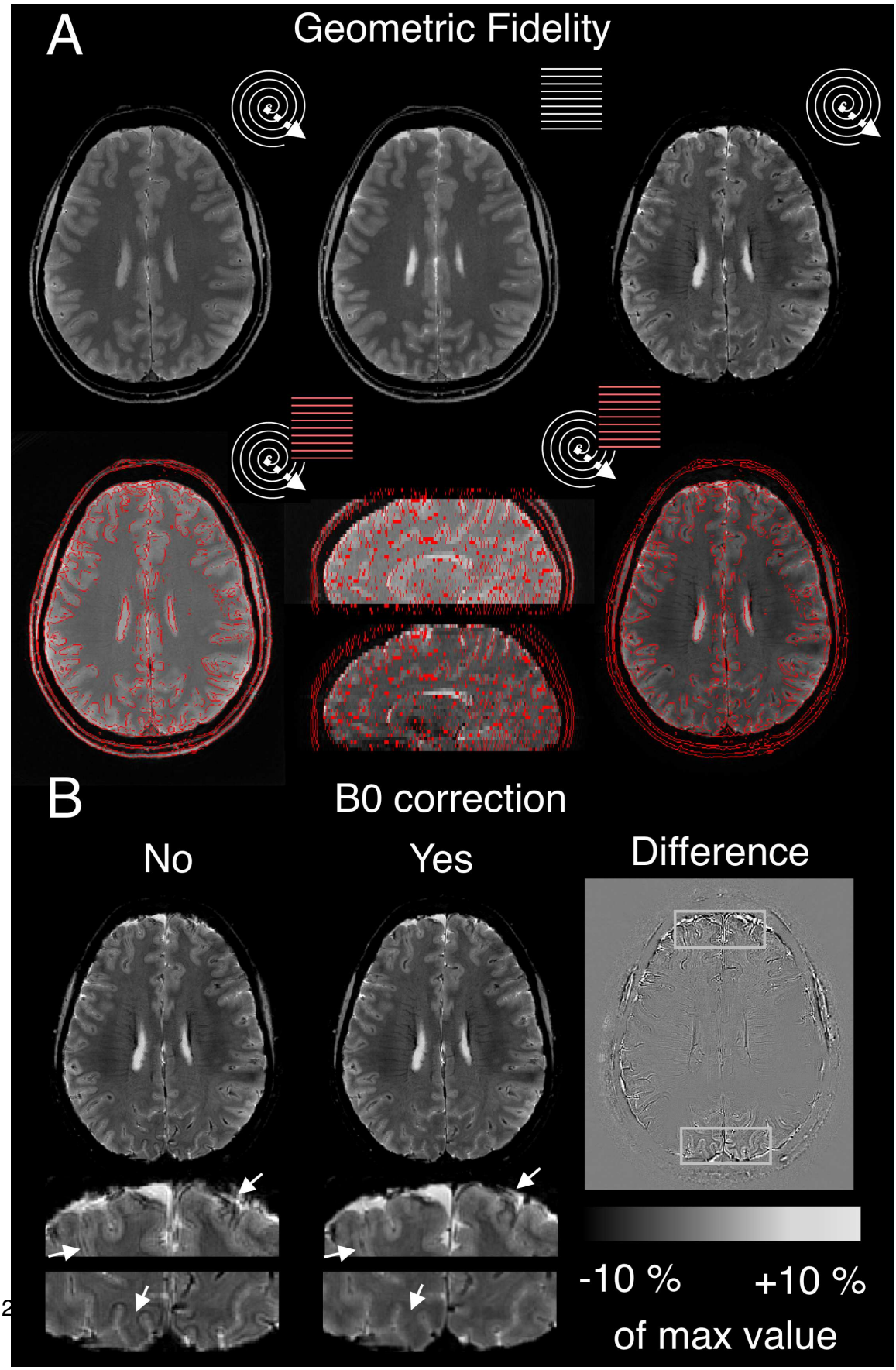
A
Geometric Fidelity
B
B0 correction
No
Yes
Difference
-10 %
+10 %
of max value

***Figure 7**: Geometric fidelity of spiral depiction and impact of expanded signal model.*

(A) Geometric comparison of spiral to Cartesian scans. (Top row) Tissue contrast, boundaries and overall brain shape match well between short-TE spiral scan (left) and Cartesian spin-warp image of same TE (middle, first echo of multi-TE scan used for reference scans). Geometric fidelity is also apparent for the long-TE spiral-out image (right). (Bottom row) Overlay of tissue borders of the spin-warp image onto both spiral images showing geometric accuracy in within-slice detail and sagittal whole-brain view. (B) Impact of static B0 correction. (Left) No B0 correction, i.e., omitting static off-resonance term in the expanded signal model, leading to edge duplication and enlarged signal voids (zooms bottom row). (Center) Reconstruction with full signal model, including B0 correction. (Right) Difference image revealing intensity changes of more than 10 % of maximum pixel value (white box = zoom position), particularly affecting high-resolution detail.

3.4 Further Acceleration

For the faster 0.7 mm spiral acquisitions, overall contrast and geometric fidelity with both spiral-in and -out scanning were similar to the 0.5 mm results with TE 25 ms (Fig. 8AB). However, some anatomical detail was lost, e.g., in delineating vessels, due to lower nominal resolution as well as somewhat longer readouts, which induced stronger T2* blurring. Furthermore, image quality was affected by stronger through-plane dephasing because of the longer TE.

With parallel imaging acceleration (SENSE factor 4, 9 s total scan time for 3 interleaves) the contrast-to-noise ratio dropped considerably, but the noise patterns did not exhibit spatial structure impairing identification of anatomical structures (Fig. 8C,D)

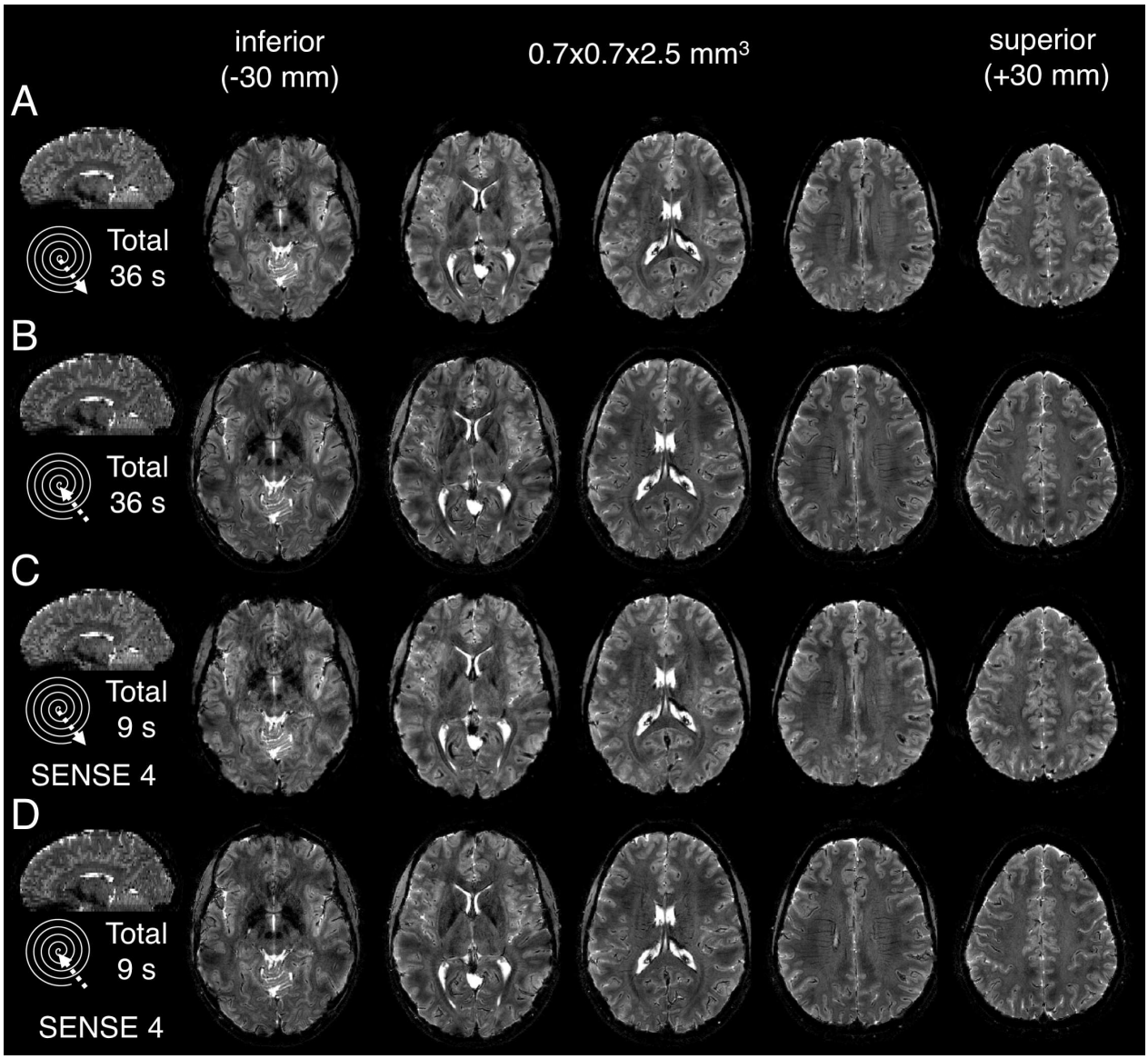

***Figure 8**: Fast spiral-out and spiral-in T2*-weighted imaging (0.7 mm) by few-shot imaging and parallel acceleration. (A) Spiral-out, TE 25 ms, T2* weighting with similar contrast to Fig. 5C; whole brain coverage in 36 s = 12 x TR. (B) Spiral-in, TE 29 ms, T2* weighting similar to Fig. 5B. (C) Spiral-out, TE 25 ms, SENSE-factor 4. As (A), but only 3 interleaves used for parallel imaging reconstruction. Resulting acquisition time for whole-brain coverage 9 s = 3 x TR, at the expense of noise enhancement, but with artifact levels comparable to the fully sampled acquisition. (D) Spiral-in, TE 29 ms, SENSE factor 4. As (B), but only 3 interleaves used.*

3.5 Intrinsic Phase Contrast

Since the reconstruction strategy employed here yields complex-valued images it includes phase information in addition to magnitude images. Inspection of the phase of spiral-out images reveals good gray/white matter contrast, deep gray matter and detailed vessel depiction, as well as few phase wraps (Fig. 9). Notably, no background field removal (e.g., high-pass filtering) or other phase preprocessing, as is common in susceptibility-weighted imaging, was performed on these images. Instead, the inclusion of static off-resonance effects into the expanded signal model intrinsically demodulated the image phase at the level of resolution supported by the B0 maps.

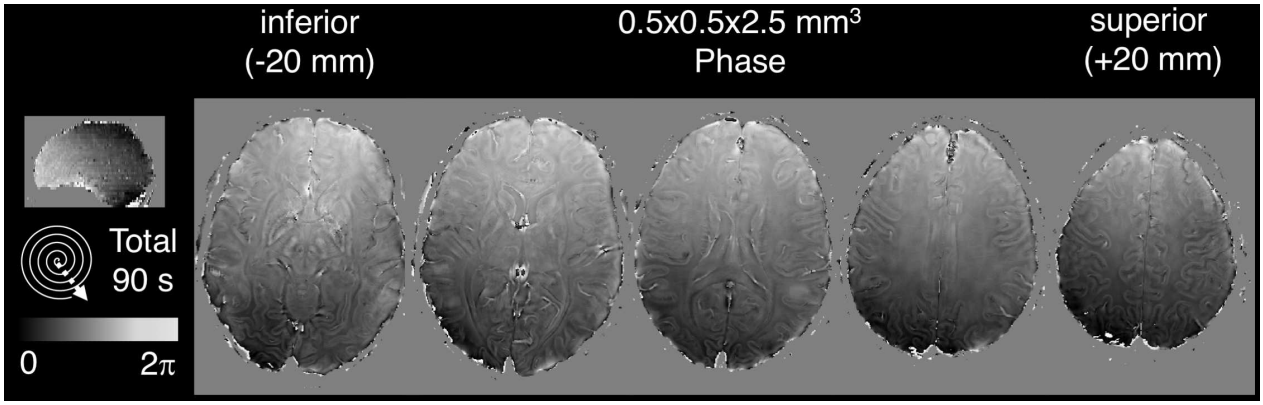

***Figure 9**: Intrinsic phase contrast of spiral-out images (resolution 0.5 mm, TE 25 ms, corresponding magnitude images in Fig. 5C). Deep gray matter structures (e.g., red nucleus, thalamus), cortical gray/white matter boundaries and vessel architecture are well discernible. Note that the phase is presented without any pre-processing since B0-corrected reconstruction accounts for off-resonance to the degree represented in the B0 maps.*

4 Discussion

In this work, spiral acquisition has been found to be a competitive candidate for anatomical MR imaging. The quality and geometric fidelity of the presented spiral images are comparable to conventional spin-warp images, acquired at a fraction of the scan time (acceleration factors of 5-

10). Structural T_2^* images with 0.5 mm in-plane resolution were obtained in 1.5 minutes, achieving whole-brain coverage for a slice thickness of about 2-3 mm. This protocol might be interesting for clinical applications, such as the study of microbleeds, where 2D acquisition schemes still dominate (Greenberg et al., 2009), due to their relative insensitivity to flow and movement artifacts, and the more flexible selection of target regions compared to 3D, where foldover in the third dimension typically also requires slab oversampling, reducing acquisition efficiency.

Parallel-imaging acceleration was readily available with the SENSE-based reconstruction approach. At an undersampling factor of 3, contrast and anatomical detail of T2*-weighted images were essentially preserved, reducing the overall acquisition time to 30 seconds for whole-brain coverage.Spiral-in and long-TE spiral-out trajectories provided similar T2*-weighted contrast at a high resolution of 0.5 mm. For highest overall imaging speed, spiral-in trajectories are preferable as they finish sooner, at TE. Corresponding phase images, due to background field removal intrinsic to the reconstruction approach, permit direct application in susceptibility-weighted imaging and quantitative susceptibility mapping (QSM). The short-TE spiral-out sequence offered an alternative contrast with clear gray/white matter differentiation, at higher SNR and less through-plane dephasing than the long-TE spirals. However, it exhibited slight residual ringing close to the skull, which arises from incomplete fat suppression.

Robust spiral imaging was enabled by use of an expanded signal model encompassing actual gradient and B0 dynamics as well as maps of static off-resonance and coil sensitivities, in combination with algebraic reconstruction.

4.1 Limitations

At the field strength of 7T, limitations were encountered at long TE and with very long spiral readouts of 25 ms and above, leading to the onset of blurring and shading artefacts as well as patches of amplified noise. The chief underlying issue is signal dephasing, which poses two challenges to the signal model and its inversion. Firstly, dephasing is intrinsically hard to include in a signal model for image reconstruction as it involves intra-voxel processes at a spatial scale that the respective scan is incapable of resolving. Secondly, even when properly reflected by a

signal model, dephasing tends to give rise to adverse conditioning of the associated inverse problem, boosting detection noise as well as systematic model errors. Furthermore, excessively long readouts might be unfavorable for other reasons as well, such as the broadening of the point-spread function due to T_2* decay. The robust cases of readout durations up to 20 ms or shorter TE still indicate a large feasible regime of spiral sequence parameters in which signal formation can be properly described and inverted.

4.2 Prospective Applications

The present work is limited to spiral readouts in gradient echo imaging. However, spiral readout modules can be equally used to improve the acquisition speed and duty cycle of other sequences. They are particularly effective in techniques with significant overhead such as inversion-recovery, multi-spin-echo, or diffusion-weighted scans. Besides structural imaging, spiral acquisition with single-shot readouts at slightly lower resolution is attractive for functional MRI, primarily for BOLD (Glover, 2012) and ASL (Detre et al., 2012) contrast, but also for functional QSM (Balla et al., 2014).

At lower field strengths such as 3 T the favorable regime of sequence parameters for the expanded signal model is expected to be even larger as susceptibility-induced dephasing is reduced at all length scales. Substantially longer spiral readout durations are conceivable and thus even higher acquisition duty cycles.

The approach used here is not restricted to Archimedean spiral trajectories since the corrections introduced by the expanded signal model work regardless of specific assumptions on gradient waveforms. The method can thus be applied to the realm of trajectory optimization, for example, for enabling variable-density spirals for SNR-optimal or artifact-suppressing acquisition (Kasper et al., 2015; Tsai and Nishimura, 2000).

Similarly, the method can be readily extended to simultaneous multi-slice or 3D acquisitions, such as stack of spirals (Deng et al., 2016; Engel et al., 2017; Zahneisen et al., 2014) or arbitrary 3D trajectories (Pipe et al., 2011; Zahneisen et al., 2012). 3D offers the advantages of insensitivity to slice profile inaccuracies and isotropic voxel size without gaps, and the combined SNR benefits of 3D averaging and high field render it particularly attractive for ultra-high

resolution applications. The signal model employed here makes no intrinsic 2D assumption, and the good performance of the approach suggests it should work as well in 3D. Reconstruction time and memory requirements, however, increase considerably compared to a single slice, because the data objects handled by the iterations become bigger. Compared to the reconstruction time of all 2D slices taken together, gridding and FFT operations are of the same complexity in 3D (apart from a constant scaling factor for gridding kernel width and grid oversampling factor in the third dimension, respectively, see (Beatty et al., 2005, pp. 800–801), and MFI will need considerably more time, because it interpolates the frequency range of the whole 3D volume of the B0 map, as opposed to the typically smaller range within a 2D slice.

4.3 Alternative Data for Expanded Signal Model

The expanded signal model is critical for reconstructing high-quality images but its components can be determined in various ways. Static off-resonance and coil sensitivity maps were derived from a separate multi-echo spin-warp reference scan here. Scan times can be reduced to below one minute by reducing spatial resolution from one to several millimeters. For coil sensitivity estimation, this is well justified by their overall spatial smoothness. For static offresonance maps, the variational algorithm used in their post-processing filtered high-resolution detail by enforcing spatial smoothness over several voxels.

Auto-calibration data can replace reference scans, e.g. the densely sampled k-space center in variable density spirals. This data may serve as input to an initial low-resolution image reconstruction to estimate coil sensitivities, or lend itself to more sophisticated non-linear reconstruction methods, for example, joint estimation of image and reference maps in a single reconstruction (Hernando et al., 2008; Sutton et al., 2004; Uecker et al., 2008). Using multi-echo spiral acquisition, this approach may extend to static off-resonance map estimation, at the cost of additional scan time, and additional water/fat separation (Hernando et al., 2008; Wang et al., 2016), as an alternative to fat suppression.

The encoding field dynamics, as a second critical component of the expanded signal model, can be readily measured by concurrent field monitoring, which is perhaps the most principled but

401 also a technically demanding approach. For reproducible deviations from prescribed encoding
402 (for example, induced by eddy currents), non-concurrent techniques are suitable alternatives.
403 These include measuring the field dynamics in a separate experiment (pre-calibration, (Duyn et
404 al., 1998; Mason et al., 1997; Tan and Meyer, 2009)), or characterizing the gradient response to
405 any input demand waveform, e.g. as a linear time-invariant system (gradient impulse response
406 function, GIRF, (Addy et al., 2012; Campbell-Washburn et al., 2016; Vannesjo et al., 2013, 2014,
407 2016b)). Irreproducible field modulations, for example, due to breathing or gradient heating,
408 typically exhibit a much lower bandwidth (< 1Hz). Here, navigator-based techniques can be
409 used, at the cost of reducing the acquisition duty cycle. Recently, model-based approaches
410 based on peripheral measures and training data have been proposed as well, for example GIRF
411 updates based on external temperature sensor readouts (Dietrich et al., 2016b), or field
412 estimates from breathing belt time courses (Vannesjo et al., 2016a).

413 4.4 Complementary Improvements

414 To further the feasible application regime of the expanded signal model, one has to target the
415 limitations set by signal dephasing, either by reducing the static field inhomogeneity as its
416 source, or improving the accuracy of the signal model describing it.

417 For reducing static field inhomogeneity, advanced active shimming techniques may provide a
418 better conditioning of the reconstruction problem, e.g. slice-wise shimming for 2D imaging as
419 employed here (Fillmer et al., 2016; Morrell and Spielman, 1997; Sengupta et al., 2011;
420 Vannesjo et al., 2017).

421 The accuracy of the signal model can be improved both for static and dynamic encoding fields to
422 capture dephasing. Higher-order field dynamics, though measured by concurrent field
423 monitoring, were not considered for image reconstruction here, as their overall contribution to
424 the phase evolution was small. Inversion including higher order field components, however, can
425 be done with minimal changes to the image reconstruction algorithm (Wilm et al., 2011),
426 forfeiting reconstruction acceleration by multi-frequency interpolation and gridding, and has been
427 successfully applied to spiral diffusion imaging as well (Wilm et al., 2017). The higher
428 computational costs (due to the direct matrix-vector multiplications) can be covered by GPU-

based reconstruction (Bieri et al., 2011), or MFI-like approximations to the encoding phase term (Wilm et al., 2012).

With respect to static off-resonance, inaccuracies of the signal model mainly stem from geometric mis-registration between reference maps and spiral acquisition, as induced by subject motion. Map co-registration or updates to the reference maps via low-resolution spiral navigators could provide a partial solution here. Prospective motion correction constitute a more comprehensive approach (Maclaren et al., 2013), and can be combined with field monitoring, e.g., using head-mounted NMR field probes (Aranovitch et al., 2016; Haeberlin et al., 2015).

5 Conclusion

The results of this work indicate that spiral readouts are a competitive option for structural MRI and form an effective means of converting enhanced sensitivity at high field into imaging speed. The chief challenges to spiral imaging, static off-resonance and dynamic field imperfections, have been addressed by inclusion in the signal model used for image reconstruction. With this approach, readout lengths of multiple tens of ms have been found to be manageable at 7T, permitting rapid structural imaging with high geometric consistency.

6 ACKNOWLEDGMENTS

This work was supported by the NCCR “Neural Plasticity and Repair” at ETH Zurich and the University of Zurich (LK, KPP, KES), the René and Susanne Braginsky Foundation (KES), and the University of Zurich (KES). Technical support from Philips Healthcare, Best, The Netherlands, is gratefully acknowledged.

7 REFERENCES

Addy, N.O., Wu, H.H., Nishimura, D.G., 2012. A Simple Method for MR Gradient System Characterization and k-Space Trajectory Estimation. Magn. Reson. Med. Off. J. Soc. Magn. Reson. Med. Soc. Magn. Reson. Med. 68, 120–129. doi:10.1002/mrm.23217

Ahn, C.B., Kim, J.H., Cho, Z.H., 1986. High-Speed Spiral-Scan Echo Planar NMR Imaging-I. IEEE Trans. Med. Imaging 5, 2–7. doi:10.1109/TMI.1986.4307732

Aranovitch, A., Haeberlin, M., Gross, S., Schmid, T., Pruessmann, K.P., 2016. Prospective Motion Correction With NMR Markers Using Only Native Sequence Elements, in: Proc. Intl. Soc. Mag. Reson. Med. 24. Presented at the ISMRM, Singapore, Singapore, p. 101.

Ashburner, J., Friston, K.J., 2005. Unified segmentation. NeuroImage 26, 839–851. doi:10.1016/j.neuroimage.2005.02.018

Balla, D.Z., Sanchez-Panchuelo, R.M., Wharton, S.J., Hagberg, G.E., Scheffler, K., Francis, S.T., Bowtell, R., 2014. Functional quantitative susceptibility mapping (fQSM). NeuroImage 100, 112–124. doi:10.1016/j.neuroimage.2014.06.011

Bammer, R., Auer, M., Keeling, S.L., Augustin, M., Stables, L.A., Prokesch, R.W., Stollberger, R., Moseley, M.E., Fazekas, F., 2002. Diffusion tensor imaging using single-shot SENSE-EPI. Magn. Reson. Med. 48, 128–136. doi:10.1002/mrm.10184

Barmet, C., De Zanche, N., Pruessmann, K.P., 2008. Spatiotemporal magnetic field monitoring for MR. Magn. Reson. Med. 60, 187—197.

Barmet, C., De Zanche, N., Wilm, B.J., Pruessmann, K.P., 2009. A transmit/receive system for magnetic field monitoring of in vivo MRI. Magn. Reson. Med. 62, 269–276. doi:10.1002/mrm.21996

Barmet, C., Tsao, J., Pruessmann, K.P., 2005. Sensitivity encoding and BO inhomogeneity–A simultaneous reconstruction approach, in: Proceedings of the ISMRM. p. 682.

Barmet, C., Tsao, J., Pruessmann, K.P., 2004. Efficient iterative reconstruction for MRI in strongly inhomogeneous B0, in: Proceedings of the 13th Annual Meeting of ISMRM, Miami. p. 347.

Barmet, C., Wilm, B.J., Pavan, M., Katsikatsos, G., Keupp, J., Mens, G., Pruessmann, K.P., 2010. Concurrent higher-order field monitoring for routine head MRI: an integrated heteronuclear setup, in: Proc. Intl. Soc. Mag. Reson. Med. 18. Presented at the ISMRM, Stockholm, p. 216.

Beatty, P.J., Nishimura, D.G., Pauly, J.M., 2005. Rapid gridding reconstruction with a minimal oversampling ratio. IEEE Trans. Med. Imaging 24, 799—808.

Bernstein, M.A., Zhou, X.J., Polzin, J.A., King, K.F., Ganin, A., Pelc, N.J., Glover, G.H., 1998. Concomitant gradient terms in phase contrast MR: Analysis and correction. Magn. Reson. Med. 39, 300–308. doi:10.1002/mrm.1910390218

Bieri, M.A., Barmet, C., Wilm, B.J., Pruessmann, K.P., 2011. Versatile Higher-Order Reconstruction Accelerated by a Graphics Processing Unit (GPU), in: Proc. Intl. Soc. Mag. Reson. Med. 19. Presented at the ISMRM, Montreal, Canada, p. 2545.

Block, K.T., Frahm, J., 2005. Spiral imaging: A critical appraisal. J. Magn. Reson. Imaging 21, 657–668. doi:10.1002/jmri.20320

Börnert, P., Schomberg, H., Aldefeld, B., Groen, J., 1999. Improvements in spiral MR imaging. Magn. Reson. Mater. Phys. Biol. Med. 9, 29–41. doi:10.1007/BF02634590

Campbell-Washburn, A.E., Xue, H., Lederman, R.J., Faranesh, A.Z., Hansen, M.S., 2016. Real-time distortion correction of spiral and echo planar images using the gradient system impulse response function. Magn. Reson. Med. 75, 2278–2285. doi:10.1002/mrm.25788

De Zanche, N., Barmet, C., Nordmeyer-Massner, J.A., Pruessmann, K.P., 2008. NMR probes for measuring magnetic fields and field dynamics in MR systems. Magn. Reson. Med. 60, 176—186.

Deng, W., Zahneisen, B., Stenger, V.A., 2016. Rotated stack-of-spirals partial acquisition for rapid volumetric parallel MRI. Magn. Reson. Med. 76, 127–135. doi:10.1002/mrm.25863

Detre, J.A., Rao, H., Wang, D.J.J., Chen, Y.F., Wang, Z., 2012. Applications of arterial spin labeled MRI in the brain. J. Magn. Reson. Imaging 35, 1026–1037. doi:10.1002/jmri.23581

501 Dietrich, B.E., Brunner, D.O., Wilm, B.J., Barmet, C., Gross, S., Kasper, L., Haeberlin, M., Schmid, T.,
502 Vannesjo, S.J., Pruessmann, K.P., 2016a. A field camera for MR sequence monitoring and system
503 analysis. Magn. Reson. Med. 75, 1831–1840. doi:10.1002/mrm.25770

504 Dietrich, B.E., Reber, J., Brunner, D.O., Wilm, B.J., Pruessmann, K.P., 2016b. Analysis and Prediction of
505 Gradient Response Functions under Thermal Load, in: Proc. Intl. Soc. Mag. Reson. Med. 24.
506 Presented at the ISMRM, Singapore, Singapore, p. 3551.

507 Duerst, Y., Wilm, B.J., Dietrich, B.E., Vannesjo, S.J., Barmet, C., Schmid, T., Brunner, D.O.,
508 Pruessmann, K.P., 2015. Real-time feedback for spatiotemporal field stabilization in MR systems.
509 Magn. Reson. Med. 73, 884–893. doi:10.1002/mrm.25167

510 Duyn, J.H., Yang, Y., Frank, J.A., van der Veen, J.W., 1998. Simple correction method for k-space
511 trajectory deviations in MRI. J. Magn. Reson. 132, 150–153.

512 Engel, M., Kasper, L., Pruessmann, K.P., 2017. Rapid 3D imaging with multiplanar spirals, in: Proc. Intl.
513 Soc. Mag. Reson. Med. 25. Presented at the ISMRM, Honolulu, Hawaii, USA, p. 5541.

514 Fillmer, A., Vannesjo, S.J., Pavan, M., Scheidegger, M., Pruessmann, K.P., Henning, A., 2016. Fast
515 iterative pre-emphasis calibration method enabling third-order dynamic shim updated fMRI.
516 Magn. Reson. Med. 75, 1119–1131. doi:10.1002/mrm.25695

517 Glover, G.H., 2012. Spiral imaging in fMRI. NeuroImage, 20 YEARS OF fMRI20 YEARS OF fMRI 62,
518 706–712. doi:10.1016/j.neuroimage.2011.10.039

519 Greenberg, S.M., Vernooij, M.W., Cordonnier, C., Viswanathan, A., Salman, R.A.-S., Warach, S., Launer,
520 L.J., Van Buchem, M.A., Breteler, M.M.B., 2009. Cerebral Microbleeds: A Field Guide to their
521 Detection and Interpretation. Lancet Neurol. 8, 165–174. doi:10.1016/S1474-4422(09)70013-4

522 Haeberlin, M., Kasper, L., Barmet, C., Brunner, D.O., Dietrich, B.E., Gross, S., Wilm, B.J., Kozerke, S.,
523 Pruessmann, K.P., 2015. Real-time motion correction using gradient tones and head-mounted
524 NMR field probes. Magn. Reson. Med. 74, 647–660. doi:10.1002/mrm.25432

525 Harshbarger, T.B., Twieg, D.B., 1999. Iterative reconstruction of single-shot spiral MRI with off
526 resonance. IEEE Trans. Med. Imaging 18, 196–205. doi:10.1109/42.764889

527 Heberlein and, K., Hu, X., 2006. Auto-calibrated parallel spiral imaging. Magn. Reson. Med. 55, 619–625.
528 doi:10.1002/mrm.20811

529 Heidemann, R.M., Griswold, M.A., Seiberlich, N., Krüger, G., Kannengiesser, S.A.R., Kiefer, B.,
530 Wiggins, G., Wald, L.L., Jakob, P.M., 2006. Direct parallel image reconstructions for spiral
531 trajectories using GRAPPA. Magn. Reson. Med. 56, 317–326. doi:10.1002/mrm.20951

532 Hernando, D., Haldar, J.P., Sutton, B.P., Ma, J., Kellman, P., Liang, Z.-P., 2008. Joint estimation of
533 water/fat images and field inhomogeneity map. Magn. Reson. Med. 59, 571–580.
534 doi:10.1002/mrm.21522

535 Jackson, J.I., Meyer, C.H., Nishimura, D.G., Macovski, A., 1991. Selection of a convolution function for
536 Fourier inversion using gridding. IEEE Trans. Med. Imaging 10, 473—478.
537 doi:http://dx.doi.org/10.1109/42.97598

538 Kaldoudi, E., Williams, S.C.R., Barker, G.J., Tofts, P.S., 1993. A chemical shift selective inversion
539 recovery sequence for fat-suppressed MRI: Theory and experimental validation. Magn. Reson.
540 Imaging 11, 341–355. doi:10.1016/0730-725X(93)90067-N

541 Kasper, L., Engel, M., Barmet, C., Haeberlin, M., Wilm, B.J., Dietrich, B.E., Schmid, T., Gross, S.,
542 Brunner, D.O., Stephan, K.E., Pruessmann, K.P., 2017. T2* MR Brain Images at 7 Tesla with 0.5
543 mm In-plane Resolution and Whole-Brain Coverage in 90 seconds Enabled by Spiral Acquisition
544 and an Expanded Signal Model. Data in Brief submitted.

545 Kasper, L., Haeberlin, M., Bollmann, S., Vannesjo, S.J., Wilm, B.J., Dietrich, B.E., Gross, S., Stephan,
546 K.E., Pruessmann, K.P., 2015. Matched-filter acquisition of high-resolution single-shot spirals, in:
547 Proc. Intl. Soc. Mag. Reson. Med. 23. Presented at the ISMRM, Toronto, Canada, p. 2060.

548 Kasper, L., Haeberlin, M., Dietrich, B.E., Gross, S., Barmet, C., Wilm, B.J., Vannesjo, S.J., Brunner,
549 D.O., Ruff, C.C., Stephan, K.E., Pruessmann, K.P., 2014. Matched-filter acquisition for BOLD
550 fMRI. NeuroImage 100, 145–160. doi:10.1016/j.neuroimage.2014.05.024

551 Langkammer, C., Bredies, K., Poser, B.A., Barth, M., Reishofer, G., Fan, A.P., Bilgic, B., Fazekas, F.,
552 Mainero, C., Ropele, S., 2015. Fast quantitative susceptibility mapping using 3D EPI and total
553 generalized variation. NeuroImage 111, 622–630. doi:10.1016/j.neuroimage.2015.02.041

554 Likes, R.S., 1981. Moving Gradient Zeugmatography. 4.397.343.

555 Lustig, M., Kim, S.-J., Pauly, J.M., 2008. A Fast Method for Designing Time-Optimal Gradient
556 Waveforms for Arbitrary k-Space Trajectories. IEEE Trans. Med. Imaging 27, 866–873.
557 doi:10.1109/TMI.2008.922699

558 Maclaren, J., Herbst, M., Speck, O., Zaitsev, M., 2013. Prospective motion correction in brain imaging: A
559 review. Magn. Reson. Med. 69, 621–636. doi:10.1002/mrm.24314

560 Maeda, A., Sano, K., Yokoyama, T., 1988. Reconstruction by weighted correlation for MRI with time-
561 varying gradients. IEEE Trans. Med. Imaging 7, 26–31. doi:10.1109/42.3926

562 Man, L.C., Pauly, J.M., Macovski, A., 1997. Multifrequency interpolation for fast off-resonance
563 correction. Magn. Reson. Med. 37, 785–92. doi:9126954

564 Mansfield, P., 1977. Multi-planar image formation using NMR spin echoes. J. Phys. C Solid State Phys.
565 10, L55. doi:10.1088/0022-3719/10/3/004

566 Mason, G.F., Harshbarger, T., Hetherington, H.P., Zhang, Y., Pohost, G.M., Twieg, D.B., 1997. A Method
567 to measure arbitrary k-space trajectories for rapid MR imaging. Magn. Reson. Med. 38, 492–496.
568 doi:10.1002/mrm.1910380318

569 Meyer, C.H., Hu, B.S., Nishimura, D.G., Macovski, A., 1992. Fast Spiral Coronary Artery Imaging.
570 Magn. Reson. Med. 28, 202–213. doi:10.1002/mrm.1910280204

571 Morrell, G., Spielman, D., 1997. Dynamic shimming for multi-slice magnetic resonance imaging. Magn.
572 Reson. Med. 38, 477–483.

573 Noll, D.C., Meyer, C.H., Pauly, J.M., Nishimura, D.G., Macovski, A., 1991. A homogeneity correction
574 method for magnetic resonance imaging with time-varying gradients. IEEE Trans. Med. Imaging
575 10, 629–637. doi:10.1109/42.108599

576 Noll, D.C., Pauly, J.M., Meyer, C.H., Nishimura, D.G., Macovskj, A., 1992. Deblurring for non-2D
577 fourier transform magnetic resonance imaging. Magn. Reson. Med. 25, 319–333.
578 doi:10.1002/mrm.1910250210

579 Pipe, J.G., Zwart, N.R., Aboussouan, E.A., Robison, R.K., Devaraj, A., Johnson, K.O., 2011. A new
580 design and rationale for 3D orthogonally oversampled k-space trajectories. Magn. Reson. Med.
581 66, 1303–1311. doi:10.1002/mrm.22918

582 Poser, B.A., Ivanov, D., Tse, D.H.Y., Schaefer, A., Barth, M., Uludağ, K., 2015. High-resolution 3D EPI
583 at 7 and 9.4T and its application to quantitative susceptibility mapping, in: Proceedings of the
584 Organization for Human Brain Mapping 21. Presented at the OHBM, Honolulu, Hawaii, USA, p.
585 1577.

586 Pruessmann, K.P., 2006. Encoding and reconstruction in parallel MRI. NMR Biomed. 19, 288.
587 doi:http://dx.doi.org/10.1002/nbm.1042

588 Pruessmann, K.P., Weiger, M., Börnert, P., Boesiger, P., 2001. Advances in sensitivity encoding with
589 arbitrary k-space trajectories. Magn. Reson. Med. 46, 638—651.
590 doi:http://dx.doi.org/10.1002/mrm.1241

591 Pruessmann, K.P., Weiger, M., Scheidegger, M.B., Boesiger, P., 1999. SENSE: Sensitivity encoding for
592 fast MRI. Magn. Reson. Med. 42, 952–962. doi:10.1002/(SICI)1522-
593 2594(199911)42:5<952::AID-MRM16>3.0.CO;2-S

594 Qian, Y., Zhao, T., Hue, Y.-K., Ibrahim, T.S., Boada, F.E., 2010. High-resolution spiral imaging on a
595 whole-body 7T scanner with minimized image blurring. Magn. Reson. Med. 63, 543–552.
596 doi:10.1002/mrm.22215

597 Roemer, P.B., Edelstein, W.A., Hayes, C.E., Souza, S.P., Mueller, O.M., 1990. The NMR phased array.
598 Magn. Reson. Med. 16, 192–225. doi:10.1002/mrm.1910160203

599 Sengupta, S., Welch, E.B., Zhao, Y., Foxall, D., Starewicz, P., Anderson, A.W., Gore, J.C., Avison, M.J.,
600 2011. Dynamic B0 shimming at 7 T. Magn. Reson. Imaging 29, 483–496.
601 doi:10.1016/j.mri.2011.01.002

602 Setsompop, K., Feinberg, D.A., Polimeni, J.R., 2016. Rapid brain MRI acquisition techniques at ultra-high
603 fields. NMR Biomed. 29, 1198–1221. doi:10.1002/nbm.3478

604 Shewchuk, J.R., 1994. An Introduction to the Conjugate Gradient Method Without the Agonizing Pain.

605 Sutton, B.P., Noll, D.C., Fessler, J.A., 2004. Dynamic field map estimation using a spiral-in/spiral-out
606 acquisition. Magn. Reson. Med. 51, 1194–1204. doi:10.1002/mrm.20079

607 Sutton, B.P., Noll, D.C., Fessler, J.A., 2003. Fast, iterative image reconstruction for MRI in the presence
608 of field inhomogeneities. IEEE Trans. Med. Imaging 22, 178–188. doi:10.1109/TMI.2002.808360

609 Tan, H., Meyer, C.H., 2009. Estimation of k-space trajectories in spiral MRI. Magn. Reson. Med. 61,
610 1396–1404. doi:10.1002/mrm.21813

611 Tsai, C.-M., Nishimura, D.G., 2000. Reduced aliasing artifacts using variable-density k-space sampling
612 trajectories. Magn. Reson. Med. 43, 452–458. doi:10.1002/(SICI)1522-
613 2594(200003)43:3<452::AID-MRM18>3.0.CO;2-B

614 Uecker, M., Hohage, T., Block, K.T., Frahm, J., 2008. Image reconstruction by regularized nonlinear
615 inversion—Joint estimation of coil sensitivities and image content. Magn. Reson. Med. 60, 674–
616 682. doi:10.1002/mrm.21691

617 Van de Moortele, P.-F., Pfeuffer, J., Glover, G.H., Ugurbil, K., Hu, X., 2002. Respiration-induced B0
618 fluctuations and their spatial distribution in the human brain at 7 Tesla. Magn. Reson. Med. 47,
619 888–895. doi:10.1002/mrm.10145

620 Vannesjo, S.J., Dietrich, B.E., Pavan, M., Brunner, D.O., Wilm, B.J., Barmet, C., Pruessmann, K.P., 2014.
621 Field camera measurements of gradient and shim impulse responses using frequency sweeps.
622 Magn. Reson. Med. 72, 570–583. doi:10.1002/mrm.24934

623 Vannesjo, S.J., Duerst, Y., Vionnet, L., Dietrich, B.E., Pavan, M., Gross, S., Barmet, C., Pruessmann,
624 K.P., 2017. Gradient and shim pre-emphasis by inversion of a linear time-invariant system model.
625 Magn. Reson. Med. n/a-n/a. doi:10.1002/mrm.26531

626 Vannesjo, S.J., Eippert, F., Kong, Y., Clare, S., Miller, K.L., Tracey, I., 2016a. Breathing-induced B0 field
627 fluctuations in the cervical spinal cord at 7T, in: Proc. Intl. Soc. Mag. Reson. Med. 24. Presented
628 at the ISMRM, Singapore, Singapore, p. 49.

629 Vannesjo, S.J., Graedel, N.N., Kasper, L., Gross, S., Busch, J., Haeberlin, M., Barmet, C., Pruessmann,
630 K.P., 2016b. Image reconstruction using a gradient impulse response model for trajectory
631 prediction. Magn. Reson. Med. 76, 45–58. doi:10.1002/mrm.25841

632 Vannesjo, S.J., Haeberlin, M., Kasper, L., Pavan, M., Wilm, B.J., Barmet, C., Pruessmann, K.P., 2013.
633 Gradient system characterization by impulse response measurements with a dynamic field camera.
634 Magn. Reson. Med. 69, 583–93. doi:10.1002/mrm.24263

635 Vannesjo, S.J., Wilm, B.J., Duerst, Y., Gross, S., Brunner, D.O., Dietrich, B.E., Schmid, T., Barmet, C.,
636 Pruessmann, K.P., 2015. Retrospective correction of physiological field fluctuations in high-field
637 brain MRI using concurrent field monitoring. Magn. Reson. Med. 73, 1833–1843.
638 doi:10.1002/mrm.25303

639 Wang, D., Zwart, N.R., Li, Z., Schär, M., Pipe, J.G., 2016. Analytical three-point Dixon method: With
640 applications for spiral water–fat imaging. Magn. Reson. Med. 75, 627–638.
641 doi:10.1002/mrm.25620

642 Wilm, B.J., Barmet, C., Gross, S., Kasper, L., Vannesjo, S.J., Haeberlin, M., Dietrich, B.E., Brunner,
643 D.O., Schmid, T., Pruessmann, K.P., 2017. Single-shot spiral imaging enabled by an expanded
644 encoding model: Demonstration in diffusion MRI. Magn. Reson. Med. 77, 83–91.
645 doi:10.1002/mrm.26493

646 Wilm, B.J., Barmet, C., Pavan, M., Pruessmann, K.P., 2011. Higher order reconstruction for MRI in the
647 presence of spatiotemporal field perturbations. Magn. Reson. Med. 65, 1690–1701.
648 doi:10.1002/mrm.22767

649 Wilm, B.J., Barmet, C., Pruessmann, K.P., 2012. Fast Higher-Order MR Image Reconstruction Using
650 Singular-Vector Separation. IEEE Trans. Med. Imaging 31, 1396–1403.
651 doi:10.1109/TMI.2012.2190991

652 Wilm, B.J., Nagy, Z., Barmet, C., Vannesjo, S.J., Kasper, L., Haeberlin, M., Gross, S., Dietrich, B.E.,
653 Brunner, D.O., Schmid, T., Pruessmann, K.P., 2015. Diffusion MRI with concurrent magnetic
654 field monitoring. Magn. Reson. Med. 74, 925–933. doi:10.1002/mrm.25827

655 Yeh, E.N., Stuber, M., McKenzie, C.A., Botnar, R.M., Leiner, T., Ohliger, M.A., Grant, A.K., Willig-
656 Onwuachi, J.D., Sodickson, D.K., 2005. Inherently self-calibrating non-cartesian parallel imaging.
657 Magn. Reson. Med. 54, 1–8. doi:10.1002/mrm.20517

658 Zahneisen, B., Hugger, T., Lee, K.J., LeVan, P., Reisert, M., Lee, H.-L., Assländer, J., Zaitsev, M.,
659 Hennig, J., 2012. Single shot concentric shells trajectories for ultra fast fMRI. Magn. Reson. Med.
660 68, 484–494. doi:10.1002/mrm.23256

661 Zahneisen, B., Poser, B.A., Ernst, T., Stenger, A.V., 2014. Simultaneous Multi-Slice fMRI using spiral
662 trajectories. NeuroImage 92, 8–18. doi:10.1016/j.neuroimage.2014.01.056

663 Zwanenburg, J.J.M., Versluis, M.J., Luijten, P.R., Petridou, N., 2011. Fast high resolution whole brain
664 T2* weighted imaging using echo planar imaging at 7 T. NeuroImage 56, 1902–1907.
665 doi:10.1016/j.neuroimage.2011.03.046

666

667